Reducing Gases Triggered Cathode Surface Reconstruction for Stable Cathode-Electrolyte Interface in Practical All-Solid-State Lithium Batteries

Bingkai Zhang,[1,2] Zhiwei He,[1] Tiefeng Liu,[3] Zeheng Li,[3,] Shaojian Zhang,[1] Wenguang Zhao,[4] Zu-Wei Yin,[4] Zengqing Zhuo,[5] Mingjian Zhang,[6] Feng Pan,[4] Shanqing Zhang,[1,2] Zhan Lin[1,2*] and Jun Lu[3,*]*

[1]Guangdong Provincial Key Laboratory of Plant Resources Biorefinery, School of Chemical Engineering and Light Industry, Guangdong University of Technology, Guangzhou 510006, China.

[2]Jieyang Branch of Chemistry and Chemical Engineering Guangdong Laboratory, Jieyang 515200, P. R. China.

[3]College of Chemical and Biological Engineering, Zhejiang University, Hangzhou 310058, China.

[4]School of Advanced Materials, Peking University, Shenzhen Graduate School, Shenzhen 518055, China.

[5]Advanced Light Source, Lawrence Berkeley National Laboratory, Berkeley, CA, 94720, USA.

[6]School of Science and Engineering, The Chinese University of Hong Kong, Shenzhen 518172, China.

E-mail: 11728048@zju.edu.cn, zhanlin@gdut.edu.cn & junzoelu@zju.edu.cn

Abstract: The interfacial compatibility between cathode materials and sulfide solid-electrolytes (SEs) is a critical limiting factor of electrochemical performance in all-solid-state lithium-ion batteries (ASSLBs). In response to this challenge, this work presents a novel approach: the development of a gas-solid interface reduction reaction (GSIRR). This GSIRR process aims to mitigate the reactivity of surface oxygen by inducing a surface reconstruction layer (SRL) through an in-situ generated metal oxide on the surface of layered oxide cathode's surface. Experimental results exhibit a substantial reduction in interfacial side reactions with sulfide SEs, leading to a notable decrease in interface resistance. A specific example involves the application of a SRL, CoO/Li_2CO_3, onto $LiCoO_2$ (LCO) cathode. This modification results in impressive outcomes, including high capacity (149.7 mAh g^{-1}), remarkable cyclability (retention of 84.63% over 400 cycles at 0.2C), outstanding rate capability (86.1 mAh g^{-1} at 2C), and exceptional stability in high-loading cathode (28.97 and 23.45 mg cm^{-2}) within

This article has been accepted for publication and undergone full peer review but has not been through the copyediting, typesetting, pagination and proofreading process, which may lead to differences between this version and the Version of Record. Please cite this article as doi: 10.1002/adma.202305748.

ASSLBs. Furthermore, the SRL CoO/Li_2CO_3 enhances the interfacial stability between LCO and $Li_{10}GeP_2S_{12}$ as well as Li_3PS_4 SEs. Significantly, our experiments suggest that the GSIRR mechanism can be broadly applied, not only to LCO cathodes but also to $LiNi_{0.8}Co_{0.1}Mn_{0.1}O_2$ cathodes and other reducing gases like H_2S and CO, indicating its practical universality. This study highlights the significant influence of the surface chemistry of the oxide cathode on interfacial compatibility, and introduces a surface reconstruction strategy based on the GSIRR process as a promising avenue for designing enhanced ASSLBs.

1. Introduction

Driven by the safety issue of traditional liquid lithium-ion batteries (LLBs), researchers have incorporated inorganic solid-electrolytes (SEs) into lithium-ion batteries (LIBs). This innovation has led to the advancement from liquid-based systems to all-solid-state lithium-ion batteries (ASSLBs)[1,2,3,4]. Notably, sulfide solid-electrolytes like Li_6PS_5Cl (LPSCl)[5,6], $Li_{10}GeP_2S_{12}$ (LGPS)[5,7] and β-Li_3PS_4 (LPS)[8] have exhibited significant potential in ASSLBs because of high ionic conductivity and mechanically soft nature[5,9,10]. Despite these advantages, sulfide SEs possess limited electrochemical windows (<2.1 V vs. Li/Li^+), and the compatibility between cathode active materials (CAM) and SEs (CAM-SE interface) remains challenging, leading to poor cycling performance of ASSLBs[11,12,13,14]. Furthermore, interphases tend to develop rapidly between oxide cathodes, particularly layered $LiTMO_2$ (TM = Co, Ni, Mn), $LiNi_{0.8}Co_{0.1}Mn_{0.1}O_2$ (NCM811), and sulfide SEs, further complicating matters and earing the designation of a "black box" in solid-solid interfacial chemistry[14,15,16]. Consequently, the integration of a thin interface layer that ensures stability between CAM and SE (depicted in **Figure S1**a) has been proposed to address these challenges. Unfortunately, the procedure indeed aggrandizes the complexity of preparing technology with extra cost. Therefore, the pursuit of a stable and compatible CAM/sulfide SEs interface through interfacial optimization without resorting the use of a thin interface layer (as illustrated in **Figure S1**b), emerges as an exceedingly significant and formidable task in the realm of ASSLBs[16].

Currently, typical acidic oxides like Li_3PO_4[17], $LiNbO_3$[18], and $Li_4Ti_5O_{12}$[19] are employed to create an environment where lithium potential is the intermediate state between that of the oxide cathode and the sulfide SE and smoothing chemical potential difference at the interface. This arrangement helps in mitigating the chemical potential disparity at the interface. These oxides are applied as coatings onto cathode oxide materials using methods ranging from wet chemical techniques to advanced physical processes[20, 21]. Nonetheless, achieving a uniform, dense, and intimate coating layer on the surface of active cathode material remains challenging. This challenge is further compounded by the interplay of two-phase interfacial energy, volumetric strain, and the development of cracks and delamination during repetitive cycling (refer to **Figure S2**a). Moreover, the coating layer usually leads to a compromise in the active cathode loading, which makes them challenging to satisfy commercial areal capacity promotion (always >2.5 mAh cm^{-2}, **Figure S3**). Herein, we turn our attention to "in-situ phase transition induced coating", which can enhance the structural matching between cathode material and coating layer as well as improve their interfacial stability, and put forward a universal optimization of cathode/SE interface in ASSLBs (**Figure S2**b).

In the intrinsic structure of layered oxides, the local atomic coordination surrounding oxygen is comprised of three linear Li–O–TM configurations[22]. Within such a configuration, oxygen electrons exhibit a higher propensity for extraction when compared to the TM–O–TM configuration commonly found in metal oxides. As a result, they display a preference for engagement in chemical redox reactions[23,24]. The surface nonstoichiometric or coordination loss configurations (such as under-coordinated oxygen ions on the edge planes, polar structure on the $LiCoO_2$ (LCO) surface, and Ni surface segregation on the NMC111 surface) would further enhance the activity for interface reaction[22,25]. Residual hydroxyl and carbonate can be formed on the surface of the layered cathode from its reaction with water and carbon dioxide in ambient air, which benefits

dense coating as well as enhanced ionic conductivity[26,27]. Therefore, a proper in-situ surface reconstruction that reduces surface activity for interface reaction through metal oxide passivation could be an effective strategy to build a stable and dense coating layer on the cathode material, which simplifies the preparation procedure without the introduction of the thin interface layer in ASSLBs[22].

Motivated by the considerations outlined above, we present a strategy based on a gas-solid interface reduction reaction (GSIRR) involving layered oxides and a reducing gas (such as H_2, CO, and H_2S gas) to enable the in-situ formation of a TMO/Li_2CO_3 layer on the CAM's surface. The schematic depiction of the GSIRR process, illustrating the interaction between layered oxides and reducing gas, is displayed in **Figure 1**a, while the detailed procedure can be found in the Experimental Section. For LCO cathode, after the GSIRR process, a uniform CoO/Li_2CO_3 surface reconstructed layer (SRL) is constructed on the LCO particles, with a mere thickness of approximately 3-5 nm. The lattice structure undergoes a seamless transition from the layered LCO to the rock-salt CoO coating layer, signifying the phase transition from LCO to CoO. This reconstructed surface on the LCO cathode (referred to as SR-LCO) exhibits a remarkable initial discharge capacity of 149.7 mAh g^{-1} with obviously reduced polarization and capacity retention of 84.63% after 400 cycles at 0.2C. Consequently, the SR-LCO cathodes, possessing elevated areal loadings (23.45 and 28.97 mg cm^{-2}), demonstrate exceptional electrochemical performance. They exhibit substantial specific capacities of 106.3 and 111.7 mAh g^{-1}, accommondating high current densities (0.5C and 0.3C), and showcase exceptional cycling stability, enduring 250 and 150 cycles, respectively. This GSIRR method's superior performance, particulary when dealing with high loadings, surpasseses that of most others, effortlessly satisfying the prerequisites for practical application (as summarized in Table S1). The achievement of ultrahigh cathode areal loadings and remarkable electrochemical performance

simultaneously is almost impossible to get in ASSLBs. Most importantly, this strategy has been extended to other reducing gases (H_2S and CO) and NCM811 cathode material. As confirmed by both experimental characterization and theoretical calculations, we attribute the improved electrochemical performance to a more stable (or less active) TMO phase, which can better stabilize sulfide-SE with fewer side reactions.

2. Results and discussion

2.1 Phase composition and structure of LCO after GSIRR process

SR-LCO samples were synthesized through the GSIRR process within a hydrogen (H_2) reductant atmosphere. The notation SR-LCO-Xmin (where X represents processing time of 5, 10, 15, and 20 minutes) distinguishes the samples resulting from varying GSIRR durations. X-ray diffraction (XRD) analysis (**Figure 1**b) coupled with 'Rietveld' refinement (**Figure S4**) reveals negligible disparities between the pristine LCO (P-LCO) and SR-LCO, barring the emergence of novel peaks at approximately 36.5°, 42.5°, and 61.6°, corresponding to the CoO phase (JCPDS No. 70-2856). These diffraction peaks' intensity progressively amplifies with prolonged reaction time. The Rietveld refinement shows that SR-LCO-10min exhibits 1.68wt.% CoO (0.89wt.% for SR-LCO-5min, 3.01wt.% for SR-LCO-15min, and 7.62wt.% for SR-LCO-20min) (**Figure 1**c). Remarkably, the lattice parameters display negligible variation after treatment, affirming the preservation of LCO's bulk crystal structure **(Figure S5**). For visual insight, scanning electron microscopy (SEM) images in **Figure S6-S7** depict the morphology of P-LCO and SR-LCO-10min particles. Both P-LCO and SR-LCO particles exhibit well-crystallized structures and smooth surfaces, with a particle diameter ranging from 4 to 5 μm.

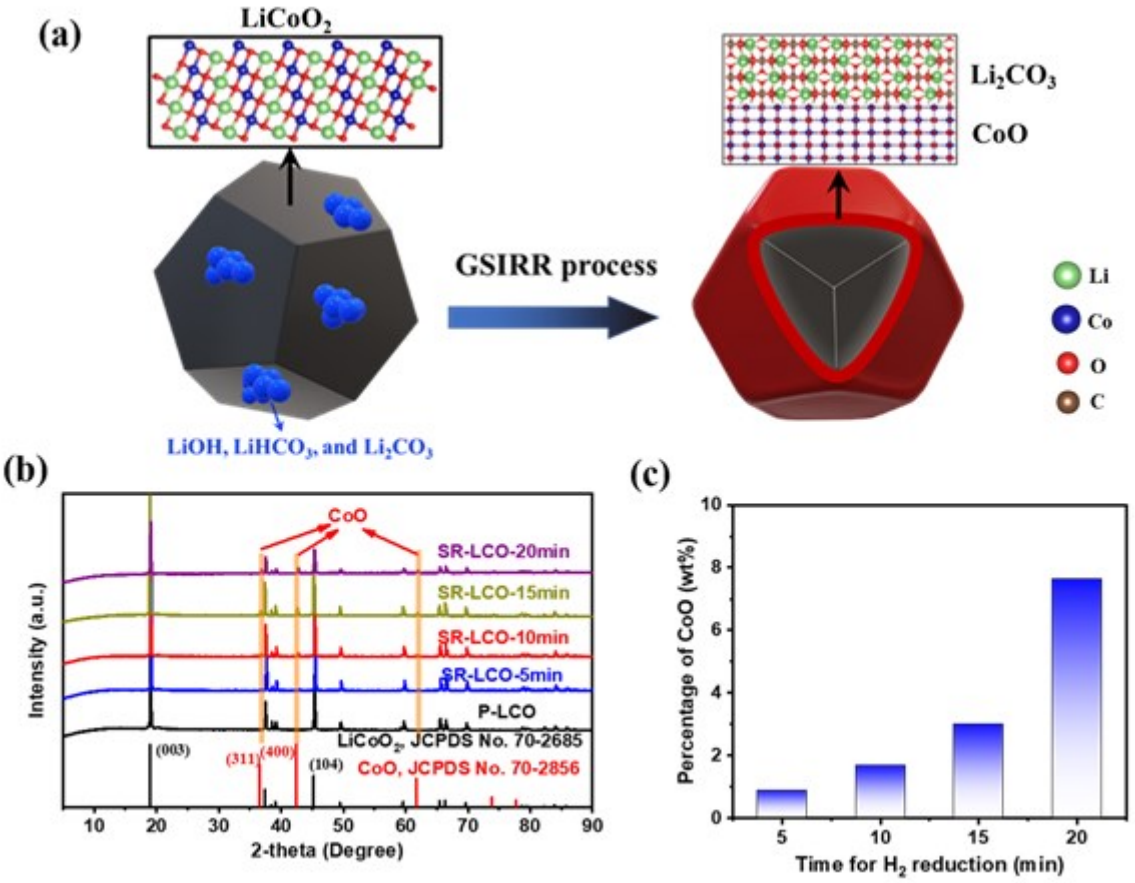

Figure 1. The formation and synthetic pathway of SRL-LCO. (**a**) Visual depiction of the GSIRR mechanism: This diagram illustrates the GSIRR process wherein oxide cathodes react with a reducing gas to form a CoO/Li_2CO_3 layer on the particle's surface. (**b**) XRD analysis of of LCO pre and post GSIRR process. (**c**) Quantifying CoO content in SR-LCO: the weight percentage (wt%) of CoO within SR-LCO composite was obtained from XRD Rietveld refinement techniques.

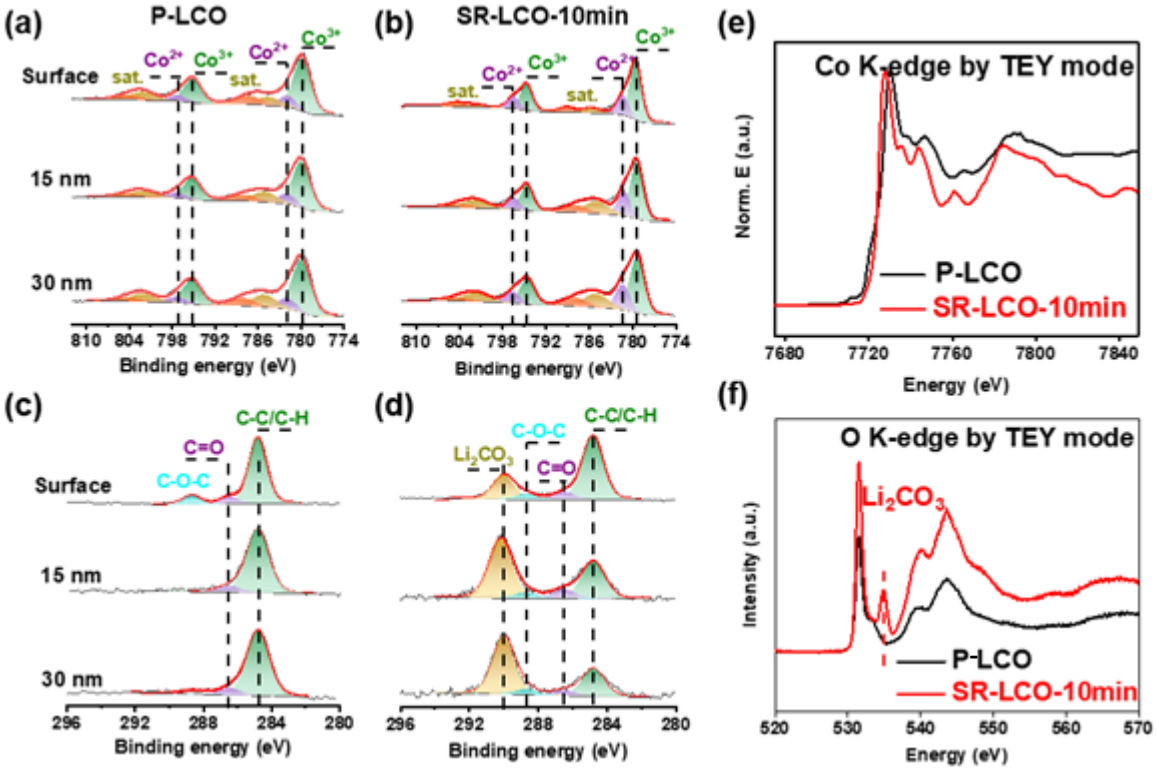

Figure 2. Surface characterizations of XPS and XAS. (**a**-**d**) XPS spectra of Co and C for the P-LCO and SR-LCO-10min samples at different depths. (**e**-**f**) X-ray absorption spectra of P-LCO and SR-LCO-10min: Co K-edge in TEY mode and O K-edge in TEY mode, respectively.

The surface composition analysis of SR-LCO-10min was further examined using spectroscopic techniques. As illustrated in **Figure 2**a-d, depth-profiling X-ray photoelectron spectroscopy (XPS) was employed to investigate the Co 2*p* and C 1*s* core spectra at different etching depth (0, 15, and 30 nm). Notably, the intensity of binding energy at 782.0/797.1 eV corresponding to bivalent cobalt (Co^{2+}), was found to be markedly higher in SR-LCO compared to P-LCO[17, 28]. This Co^{2+} content in SR-LCO was consistently greater than that observed in P-LCO across all etching depths, emphasizing its significance. For C 1*s* core peaks, the same carbon-based species are observed for both specimens: C–C/C–H groups 284.8 eV, C=O groups 286.5 eV and C–O–C 289.0 eV. It is preferred to fit this region

of the C 1*s* spectra with a single large peak (fwhm 4.0 eV) that accounts for several C–O groups that may be present within the surface, such as C–O–C, RO–CO_2Li, and $LiHCO_3$. Furthermore, a distinctive photoelectron peak was identified at 290 eV in SR-LCO, indicating the presence of carbonate (–CO_3). This stands in sharp contrast to P-LCO[29,30]. The differentiation between the two materials (SR-LCO and P-LCO) is elucidated in **Figure 2**e, which shows the Co X-ray absorption near edge structure (XANES) and extended X-ray absorption fine structure (EXAFS) of P-LCO and SR-LCO-10min. Notably, in the total electron yield (TEY) mode, a 2.0 eV energy shift towards lower values was observed in the Co K-edge threshold photon energy position for SR-LCO-10min, signifying a reduction in Co valence following GSIRR[31, 32]. Comparative analysis of Co R-space spectra from Co K-edge TEY of P-LCO and SR-LCO-10min is depicted in **Figure S8**, revealing similar bond distances for SR-LCO-10min and P-LCO (1.5 Å for Co–O and 2.4 Å for Co–Co). This similarity suggests that the GSIR process has limited impact on the bulk crystal structures of the P-LCO sample. **Figures 2**f and **S9** present the O K-edge XANES spectra of P-LCO and SR-LCO-10min in total electron yield (TEY) and total fluorescence yield (TFY) modes, respectively. A distinctive feature around ~534 eV (indicated by the red dashed line in **Figure 2**f) was exclusively observed on the surface of SR-LCO-10min, attributed to carbonate formation[30]. This feature was notably absent in the P-LCO sample within a similar energy range. Intriguingly, the carbonate feature at ~534 eV exhibited a weaker signal in the fluorescence yield (FY) mode (as shown by the red dashed line in **Figure S10**), underscoring its prevalence primarily in the surface layer. Verification of –CO_3 presence on the SR-LCO surface was further confirmed through Fourier-transform infrared spectroscopy (FTIR) analysis (**Figure S11**). To explore the electrochemical behavior, differential electrochemical mass spectrometry (DEMS) experiments were conducted on SR-LCO during cell charging (**Figure S12**). The signals indicated the decomposition of Li_2CO_3, with CO_2

evolution; however, the signal for CO_2 was relatively modest, indicating the limited presence of amorphous Li_2CO_3 in SR-LCO-10min.

To understand the nature of the surface layer, high-resolution transmission electron microscopy (HRTEM) measurements were conducted on LCO before and after the GSIRR process (**Figure 3**a). Before the TEM observation, SR-LCO-10min particles were sliced into a thin flake by Focus ion beam (FIB) technology (**Figure S13**). In the TEM image of the particle cross-section (after FIB) of **Figure 3**a, we note two different lattice fringes on SR-LCO-10min, labeled as regions A and B. Fast Fourier Transform (FFT) of region A is indexed to [100] zone of LCO phase (**Figure 3**b), while FFT of region B is indexed to [011] zone of CoO phase (**Figure 3**c). And a lattice space d_1 =4.65 Å can be indexed to (003) plane of layered LCO (JCPDS card No.70-2685), and d_2 =2.47 Å can be indexed to the (1-11) plane of rock-salt CoO (JCPDS card No.70-2685) (**Figure 3**d). No discernible phase boundary exists between the inner layered phase LCO and the outer rock-salt phase CoO, highlighting the seamless lattice coherence between the LCO core and CoO shell. And the rock-salt CoO phase layer exhibits a thickness of from 3 to 5 nm. Thus, the surface of SR-LCO-10min undergoes progressive reconstruction from an R-3m-layered structure to an Fm-3m rock-salt one. Given the pronounced –CO_3 peaks observed in XPS and XAS and the extraction of Li atoms to compensate for the changes in the phase transition of LCO → CoO, we speculate that the Li_2CO_3 phase is formed on the surface of SR-LCO. No –CO_3 diffraction peaks in XRD suggest that the amorphous region in TEM (**Figure S14**) is the Li_2CO_3 amorphous phase. Energy dispersive spectroscopy (EDS) mappings (**Figure S15**a-d) under TEM accurately indicate that the Co and O signals gather on SR-LCO-10min from surface to bulk, while a visual C signal is concentrated on the surface.

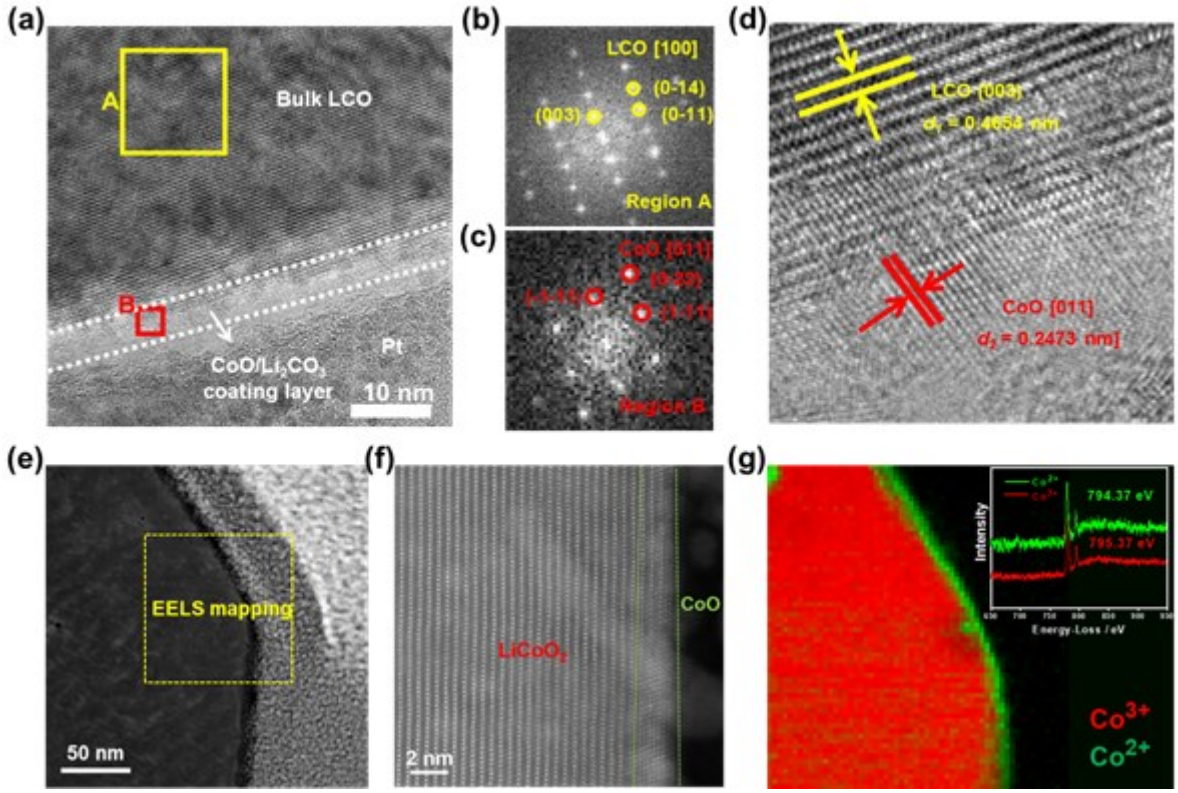

Figure 3. STEM-HAADF images and EELS analysis of SR-LCO materials. (**a**) TEM image and corresponding FFT results for region A (**b**) and region B (**c**) of SR-LCO-10min. (**d**) HR-TEM image of SR-LCO-10min sample. (**e-g**) HAADF-STEM images and EELS elemental mapping of Co^{2+} and Co^{3+}. The yellow rectangle of the STEM image indicates the analysis area. The inset in **Figure 3**g is the high-resolution EELS profile of Co^{2+} and Co^{3+}.

To gain deeper insights into the structural and valence transformations occurring within LCO during the GSIRR process, we conducted high-angle annular dark-field (HAADF)-STEM imaging and electron energy loss spectroscopy (EELS) mapping (**Figure 3**e). The electron diffraction pattern of a single SR-LCO particle unmistakably reveals the presence of a rock-salt CoO phase, which manifests as a distinct layer approximately 3 nm in thickness (**Figure 3**f), which is consistent with that observed in **Figure 3**a. The lattice patterns of both the layered LCO and the rock-salt CoO (as indicated by the

corresponding FFT patterns) are remarkably well-defined, accentuating the clear boundary demarcating these two phases. By employing multiple linear least squares (MLLS) fitting in EELS analysis, we observe in **Figure 3**g that Co^{2+} ions (highlighted in the green box) are homogeneously distributed across the particle's surface. In contrast, Co^{3+} ions (enclosed within the red box) exhibit an interior distribution. The spatial separation of these two valence states of cobalt is evident and sharply defined. The inset of **Figure 3**g provides additional validation, exhibiting the peak positions and energy shifts of Co signal. This further substantiates the coexistence of both Co^{2+} and Co^{3+} valence states subsequent to the GSIRR process. Encouragingly, the findings from the EELS analysis harmoniously align with those derived from X-ray Absorption Spectroscopy (XAS), corroborating the conclusion. In light of the congruent results obtained from XRD, XPS, XAS, and TEM investigations, we establish that the GSIRR approach seamlessly introduces a surface-reconstructed CoO/Li_2CO_3 layer with a thickness of approximately 3 to 5 nm. Notably, this introduction is accomplished without inducing any noticeable disruption to the bulk structure of the material.

2.2 Electrochemical tests of P-LCO and SR-LCO

The electrochemical performance of the SR-LCO cathode was evaluated at various C-rates and room temperature within pelletized ASSLB cells, utilizing the Li-In alloy anode and LPSCl SE. A comparative analysis was conducted against the P-LCO cathode. **Figures 4**a and **4**b depict the cycling performance and rate capability of P-LCO and different SR-LCO variants (SR-LCO-Xmin where X = 5, 10, 15, and 20) at 0.2C and 0.5C discharge rates, respectively. The cycling capacity results highlight SR-LCO-10min as the most notable performer, delivering substantial capacity and retaining impressive rate capability even after hundreds of cycles. At 0.2C, SR-LCO-10min has a higher initial capacity of 135.5 mAh g^{-1} and improved capacity retention of 87.8% after 400 cycles, compared with an initial capacity of 99.0 mAh g^{-1} and rapid degradation upon cycling for the P-LCO. Similarly, at 0.5C,

SR-LCO-10min maintains 81.7% capacity (135.2 mAh g^{-1}) after 300 cycles. **Figures S16** and **S17** illustrate the 2nd charge-discharge curves of P-LCO and SR-LCO-Xmin at 0.2C and 0.5C, respectively. Overall, SR-LCO-10min exhibits reduced voltage polarization and enhanced capacity, indicating minimized interfacial resistances with sulfide SEs. In sharp contrast, P-LCO and SR-LCO-20min exhibit significant polarization voltages and capacity deterioration. To reinforce the capacity performance of SR-LCO-10min, **Figure S18** presents its cycling stability with error bars. The rate capability analysis reinforces the superior capacity retention of SR-LCO-10min compared to other cathodes (**Figure 4**c). SR-LCO-10min can deliver >80% higher capacity at lower 0.1–0.5C rates and more than 60% higher capacity at higher 1–2C rates. Therefore, the SR-LCO with 10 minutes of thermal reduction stands out as the optimized candidate, consistently demonstrating the advantages of CoO/Li_2CO_3 SRL.

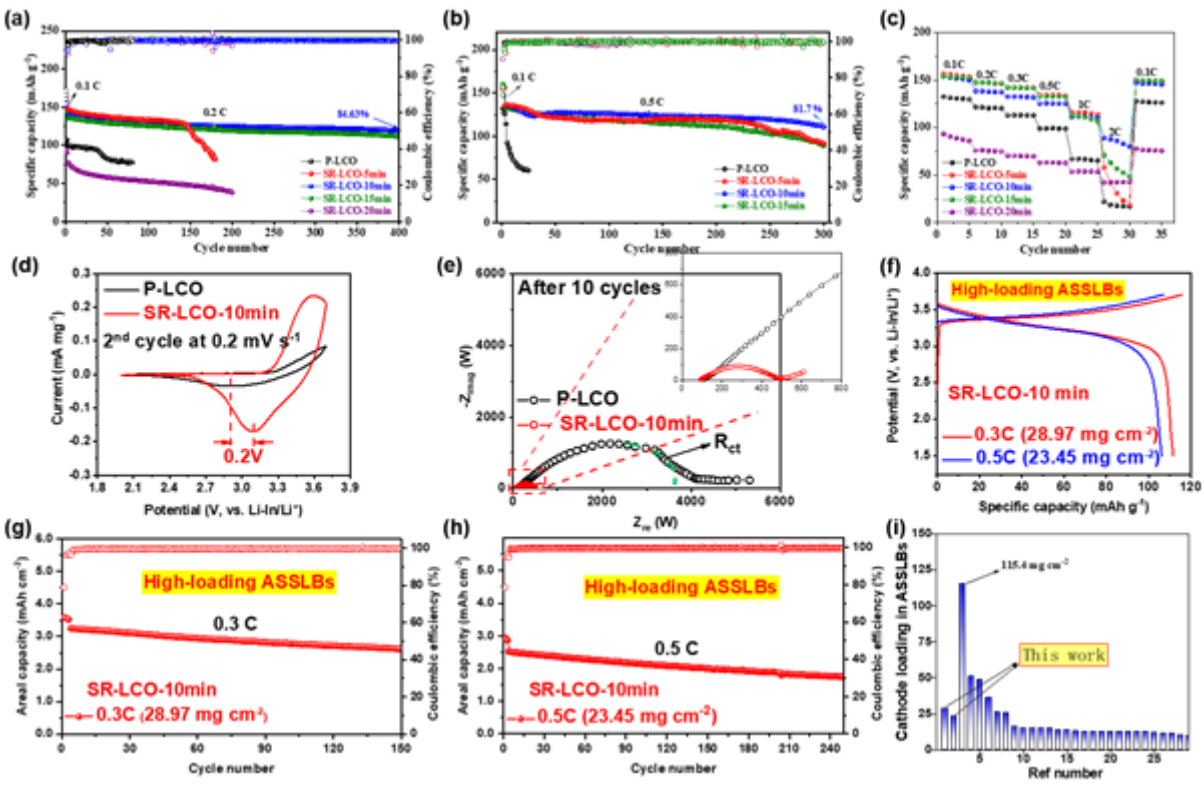

Figure 4. High-performance achieved with SR-LCO in ASSLBs. (**a**-**b**) Long-term cycling stability of batteries employing P-LCO and SR-LCO-Xmin at 0.2C and 0.5C rates, respectively. (**c**) The rate capability of ASSLBs using P-LCO and SR-LCO-10min, spanning rates from 0.1C to 2C rates. Considering the rapid degradation observed in the P-LCO cathode, we conducted tests on more than five P-LCO ASSLB cells to identify a cell sustaining a rate above the 30th cycle under high C-rate conditions. (**d**) The rate testing of batteries employing P-LCO and SR-LCO-Xmin at a scan rate of 0.2 mV s^{-1}. (**e**) The Nyquist plots of ASSLBs with P-LCO and SR-LCO after 10 cycles at 0.2C. (**f**-**h**) SR-LCO-10min ASSLBs with high loading, including the initial charge-discharge curves and the cycling performance at 0.3C and 0.5C. (**i**) The comparison of cathode areal loading in ASSLBs using the state-of-the-art ASSLBs reported in the literature. A more detailed comparison of electrochemical performance including cell design and operating conditions is shown in **Table S1**.

To better understand cycling performance associated with interfacial resistance in ASSLBs, a comprehensive set of electrochemical characterization techniques were employed on P-LCO and SR-LCO-10min cathode materials. Specifically, cyclic voltammetry (CV), galvanostatic intermittent titration technique (GITT), and electrochemical impedance spectroscopy (EIS) measurements were conducted on cells of P-LCO and SR-LCO-10min. The distinctive features of the initial capacity performance are clearly evident in the CV curves of both P-LCO and SR-LCO-10min, as illustrated in **Figures 4**d and **S19**. Notably, the current response and peak potential of oxidation and reduction processes in SR-LCO-10min present noticeable changes when compared to those observed in P-LCO. This disparity is further emphasized by the narrower half-peak width, signifying a more favorable interfacial interaction between SR-LCO-10min and LPSCl SE. The congruent trends are likewise reflected in the GITT profiles, as depicted in **Figures S20**a and **S20**b. Remarkably, SR-LCO-10min demonstrates diminished electrochemical polarization and enhanced reversibility during the

discharge process. GITT results show that Li diffusion coefficient (D_{Li}) at SR-LCO-10min is increased compared to P-LCO cathode, leading to increase in kinetics of electrochemical reactions and hence conduction of Li-ion. We calculated the ionic diffusion coefficient of the two cathode materials by the GITT and Equation 1. The Li-ion diffusion coefficient for SR-LCO-10min (5.10×10^{-14} cm^2 s^{-1}) raises more than two orders of magnitude compared to P-LCO (1.68×10^{-16} cm^2 s^{-1}). Detailed EIS analyses coupled with the fitting of an equivalent circuit model using the transmission line concept (as shown in **Figures 4**e, **S21, S22**, and **Table S2**) provide additional insights. After 10 cycles, the P-LCO cell exhibits a significant increase in resistance[33,34], with a high charge transfer resistance (R_{ct}) of 1532 Ω and a high resistance-capacitance (R_C) value of 318.5 Ω. These values unequivocally indicate a continuous deterioration of the LCO/LPSCl interface due to serious interface parasitic reactions (**Table S3**). In contrast, the integration of CoO/Li_2CO_3 contributes significantly to the stability of the interface in the SR-LCO-10min cathode. This is exemplified by the substantial reduction in the R_C parameter to 286.6 Ω and a significantly lower R_{ct} value of 118.7 Ω after 10 cycles. These outcomes strongly support the establishment of resilient solid-solid interfaces, even in the presence of intermittent physical contact at the solid-solid interfaces during cycling.

To comprehensively assess the cycling stability of SR-LCO-10min cathode, we conducted ASSLBs with significantly elevated cathode loading, as depicted in **Figure 4**f-h. When subjected to a substantial loading of 28.97 mg cm^{-2} and operated at 0.3 C, the SR-LCO-10min cathode exhibited an initial capacity of 111.7 mAh g^{-1} (equivalent to 3.24 mAh cm^{-2} areal capacity) and maintained a capacity of 94.95 mAh g^{-1} (equivalent to 2.76 mAh cm^{-2} areal capacity and 85% capacity retention) after 100 cycles (**Figure 4**g). Again, employing a higher loading of 23.45 mg cm^{-2} and operating at 0.5C, the SR-LCO-10min cathode delivered an initial capacity of 106.3 mAh g^{-1} (2.52 mAh cm^{-2} areal capacity) and exhibited a consistent capacity of 79.725 mAh g^{-1} (1.88 mAh cm^{-2} areal capacity and 75%

capacity retention) after 200 cycles (**Figure 4**h). Notably, these areal capacity values surpass the threshold of 2.5 mAh cm^{-2}, a criterion deemed essential for fulfilling the demands of high-energy-density ASSLBs, thereby augmenting its practical uses. **Figure 4**i provides a visual comparison of the current cathode areal loading achieved in this work with that of the state-of-the-art ASSLBs reported in the existing literature, with the distinctive data points for SR-LCO-10min marked within a red box. For a more comprehensive assessment encompassing electrochemical performance, encompassing cell design and operational parameters, please refer to **Table S1**. The remarkable performance of SR-LCO-10min is evident in its capability to accommodate high cathode areal loadings, coupled with proficient current density and robust cycling stability.

In addition, we also evaluated the electrochemical performance of both P-LCO and SR-LCO using liquid coin cells operating within the voltage range of 2.8–4.3 V (Li vs Li/Li^+). The charging/discharging voltage profile of SR-LCO-10min shows a slight capacity reduction with no noticeable voltage polarization (**Figure S23**). This observation suggests that CoO/Li_2CO_3 SRL as a proficient Li-ion conduction layer. **Figure S24** displays the comparative rate capacity evaluation of P-LCO and SR-LCO across a range of rates from 0.2 to 5C. The rate performance of SR-LCO-Xmin surpassed that of P-LCO, indicating remarkable improvements. Particularly noteworthy is the performance of the SR-LCO-15min cathode, which demonstrated impressive capacities of 141.36, 114.93, and 62.85 mAh g^{-1} at 0.2, 2, and 5C, respectively. Remarkably, even upon restoration to 0.2C following discharge at 5C, SR-LCO-15min exhibited a sustained discharge capacity of 141.12 mAh g^{-1}. Thus, the enhanced cycling performance in liquid cells further proves the effectiveness of the GSIRR method on LCO cathode.

2.3 ***Discussion***

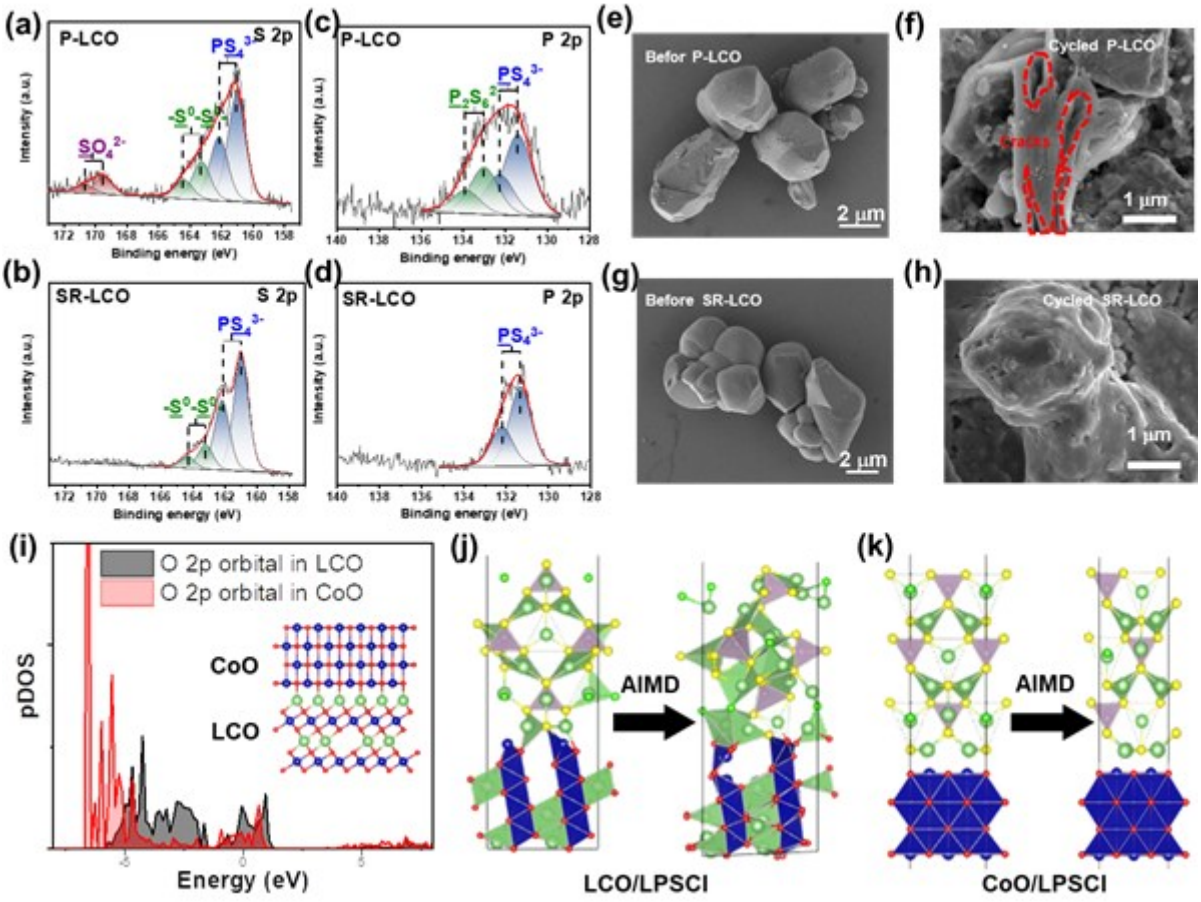

Figure 5. Revealing the interface stability with XPS, SEM, and DFT calculations. (**a**-**b**) S 2*p* and (**c**-**d**) P 2*p* XPS spectra of P-LCO/LPSCl interface and SR-LCO-10min/LPSCl interface after 10 cycles at 0.2C. (**e**-**h**) The SEM images of P-LCO and SR-LCO-10min after 10 cycles at 0.2C, respectively. (**i**) pDOS of the O 2*p* orbitals of O atoms in layered LCO coordinated by two Li and three Co, and rock-salt CoO by six Co. Inset: atomic structure of LCO/CoO interface. (**j**-**k**) The atomic structure of the LCO/LPSCl and CoO/LPSCl interface before and after 20 ps AIMD simulation.

It is natural to ask why the presence of CoO/L_2CO_3 SRL enhances the interfacial compatibility of LCO and LPSCl. To this end, we first analyzed the interphases in LCO/LPSCl sample after 10 cycles at 0.2C by XPS measurement. Shown in **Figure 5**a-d are the XPS spectra of S 2*p* and P 2*p* core-level

regions on the surface of two composite cathodes (P-LCO/LPSCl and SR-LCO/LPSCl). In the S 2*p* spectra (**Figure 5**a-b), there are three doublets of peaks for P-LCO/LPSCl sample[28,33,35,36,37]. The rightmost doublet with peaks at binding energies of 161.0 ($2p_{3/2}$) and 162.3 eV ($2p_{1/2}$) corresponds to intrinsic PS_4^{3-} structural units in LPSCl and thus appears in both samples[28,31,33,38]. The middle doublet with peaks at binding energies of 163.3 ($2p_{3/2}$) and 164.4 eV ($2p_{1/2}$) corresponds to newly-formed S–S bonds after cycling. The S–S bonds may belong to polysulfides and thiophosphate species (P_2S_x, x > 5). The leftmost doublet with peaks at binding energies of 169.5 ($2p_{3/2}$) and 170.7 eV ($2p_{1/2}$) corresponds to SO_4^{2-} structural units after cycling. It is important to note that the SO_4^{2-} peaks that existed in P-LCO/LPSCl significantly disappear in SR-LCO/LPSCl sample. Similar to P 2*p* data, there are two doublets of peaks after cycling in P-LCO/LPSCl sample. The lower binding energy doublet with peaks at binding energies of 131.4 ($2p_{3/2}$) and 132.3 eV ($2p_{1/2}$) corresponds to PS_4^{3-} structural units in LPSCl. The higher binding energy doublet with peaks at binding energies of 133.1 ($2p_{3/2}$) and 133.9 eV ($2p_{1/2}$) corresponds to newly-formed $P_2S_x^{2-}$ structural units in P-LCO/LPSCl sample. Again, the $P_2S_x^{2-}$ structural units disappear in SR-LCO/LPSCl sample. Taken together, XPS clearly demonstrates that the formation of SO_4^{2-} and $P_2S_x^{2-}$ related species is likely suppressed by CoO/Li_2CO_3 SRL in SR-LCO sample. What need reminds is, our XPS results are based on the surface of electrodes, etching a ~10 µm thick layer from the electrode surface would result in a new doublet or an intensity increase, together with the appearance of other sulfur and phosphorus environments.

Next, we examined the surface morphologies of P-LCO and SR-LCO after cycling through post-mortem scanning electron microscope (SEM) analyses. **Figure 5**e-f shows SEM images of P-LCO and SR-LCO-10min electrodes after 10 cycles at 0.2C. It can be seen that after 10 cycles, SR-LCO-10min particles are wrapped with a mellow patina or slurry-like layer (**Figure 5**f), but P-LCO particles show visible micro-cracks and an exposed layer structure (circled in red), which suggests there is a

degradation of the surface structure of the P-LCO particles (**Figure 5**e). The unstable and collapsed surface layer on P-LCO particles greatly reduces the utilization of active LCO materials after cycling. The SEM images of SR-LCO-10min after 100 cycles were also studied. As shown in **Figure S25**a-b, the LPSCl/Li-In interface structure and section of the Li-In anode preserve complete morphology with no any signs of mechanical cracking or contact loss after 100 cycles, which indicates the surface reaction between anode and solid electrolyte is not the main cause of battery failure.

To further interpret the influence of CoO/Li_2CO_3 layer on interface stability/reactivity, we performed the density functional theory (DFT) calculations from the following points of view: 1) whether or not the considered interface is thermodynamically stable in terms of phase equilibrium and oxygen reactivity calculations; and 2) when the considered interface is not thermodynamically stable, whether or not surface reaction, diffusion, and nucleation are the major kinetic factor. For the first point, the (electro)chemical stability of LPSCl and Li_2CO_3 was calculated. The DFT calculated electrochemical stability window of Li_2CO_3 overlaps with that of LPSCl. The thermodynamic oxidation limit of Li_2CO_3 is up to 4.2 V, close to the ASSLBs operating voltage window of 2.6–4.3 V vs. Li^+/Li, indicating Li_2CO_3 is likely to remain stable over the entire ASSLBs cycling.

Then, the assessment of interfacial chemical stability was conducted through computations of chemical reaction energy, elucidating thermodynamic predisposition for reaction occurrence. We note that the chemical reaction energy of LCO-LPSCl (obtained from Equation 2) is considerably higher (–0.52 eV/atom) in comparison to Li_2CO_3-LPSCl (–0.13 eV/atom), implying a greater thermodynamic stability of Li_2CO_3 when in contact with LPSCl. At the interface of LCO and LPSCl, an oxidation process ensues within LPSCl, leading to the formation of phosphates, Li_2S, Co_3S_4, Li_2SO_4, and LiCl, while the oxygen ions within LCO partake in redox reactions. Considering the strong correlation between oxygen involvement and interface compatibility during cycling, the projected

density of states (pDOS) of the oxygen 2*p* states of two oxygen environments (Co–O–Li configuration in LCO and Co–O–Co configuration in CoO) (**Figure 5**i). We found that the O 2p band center in rock-salt phase CoO is 2.75 eV lower than the O 2*p* band center of LCO. This indicates that Co–O–Co configuration in CoO shifts the depopulated O 2*p* states to lower energy and raises the O redox potential relative to that of the O redox in LCO by >2.75 V. We suggest that the strong Co–O–Co units of CoO plays a vital role in suppressing interface side reaction at SR-LCO/LPSCl interface. For the second point, we simulated the *ab initio* molecular dynamics (AIMD) of the $LiCoO_2$/LPSCl and CoO/LPSCl interface to check the interface stability. We observed that the configuration degeneration (disordered CoO_x units and the formation of S–S bonds) at the $LiCoO_2$/LPSCl interface with AIMD simulation time becomes very obvious (**Figures 5**j-k). Surprisingly, at CoO/LPSCl interface, both CoO and LSPCl maintain a complete configuration structure with respect to AIMD simulation time, indicating CoO is kinetically stable toward LPSCl SE. From the findings described above, we may infer that CoO/LPSCl has better interfacial compatibility via the less reactivity of oxygen and higher kinetic passivation effect.

Based on the phase composition/structure analysis, electrochemical cell performance, and subsequent post-processing XPS/SEM evaluations, we propose the presence of a synergy effect between Li_2CO_3 and CoO in mitigating parasitic reactions. The SRL layer significantly reduces interface resistance and enhances the interfacial stability of the cathode with sulfide SE. Within the SRL, CoO resides in the innermost layer, maintaining the crystal structural stability of LCO during the charg-discharge cycle. The amorphous Li_2CO_3 resides on the outer side of the layer, contributing to both ion conductivity and interface stability with sulfide electrolytes. Moremore, two additional factors contribute to the success of the CoO/Li_2CO_3 coating. Firstly, the CoO layer is exceptionally

thin, measuring only ~3 nm in thickness, thereby reducing the extent of the Li-ion diffusion pathway within the CoO layer. Secondly, we suggest that Li-ion diffusion through CoO coating belongs to the "space-charge model" and its transport is driven by an electric field. The CoO coating is electronically insulating, Li^+ is the only mobile species. No negative compensating charge exists in the CoO coating or the reduction of Co oxidation state, thus, a space charge develops in the CoO coating. Therefore, from the point, the dependency of the cell performance is not fully corresponded with H_2 exposure time or CoO thickness (**Figure 4**c). When H_2 exposure time is extended (**Figure S26**), that is, the content of CoO is increased, potential adverse effects of CoO and particle aggregation could hinder the sustained electrochemical performance of the SR-LCO in ASSLBs. Therefore, it is also important to choose an appropriate GSIRR process time, ensuring that the cathode material maintains optimal electrochemical performance.

2.4. Universality investigation of GSIRR method in ASSLBs

It is important to check whether SR-LCO has good interfacial compatibility with other sulfide SEs or not. We initiated our investigations by replacing the LPSCl SE with either LGPS or LPS sulfide SE in ASSLB cells. The cycling performance of LGPS-based ASSLBs is illustrated in **Figure 6**a. Remarkably, P-LCO displayed an initial capacity of 46.8 mAh g^{-1}, coupled with a steep deterioration over subsequent cycles and a notable charge/discharge voltage gap, as depicted in **Figure S27**a. In sharp contrast, the SR-LCO configuration exhibited a robust initial discharge capacity of 143.6 mAh g^{-1} at a 0.1C rate, accompanied by minimal overpotential. Its enduring cycling performance outshone expectations, with an impressive capacity retention of 85.90% after 100 cycles at 0.1C (**Figure 6**a). Analyzing the S 2*p* XPS spectra of the LCO/LGPS interface post 10 cycles revealed that the cycled SR-LCO/LGPS interface exhibited no discernible peak intensity corresponding to CoS_x. Additionally, a reduction in the intensity of S species ($–S^0–S^0–$) was observed, in contrast to the cycled P-LCO/LGPS interface

(**Figure S27**c-d). Evident in Nyquist plots, the interface resistance of P-LCO ASSLB cells ballooned to over 40,000 Ω after 10 cycles, as depicted in **Figure S27**b. Conversely, SR-LCO ASSLB cells demonstrated a significantly lower resistance with an R_c of 312.5 Ω and an R_{ct} of 260.4 Ω. Similarly, for LPS-based ASSLBs (**Figure 6**b), SR-LCO displayed a noteworthy first discharge capacity of 137.4 mAh g^{-1} at 0.1C, maintaining an 80.0% capacity retention over the course of 100 cycles. The charge/discharge voltage gap was also minimal (**Figure S28**a). Nyquist plots further elucidated the advantages of the cycled SR-LCO/LPS interface, which exhibited markedly lower resistance (~200 Ω) compared to the cycled P-LCO/LPS interface (over 4000 Ω) (**Figure S28**b). Thus, GSIRR-processed LCO exhibits good interfacial compatibility with LGPS and LPS sulfides SE.

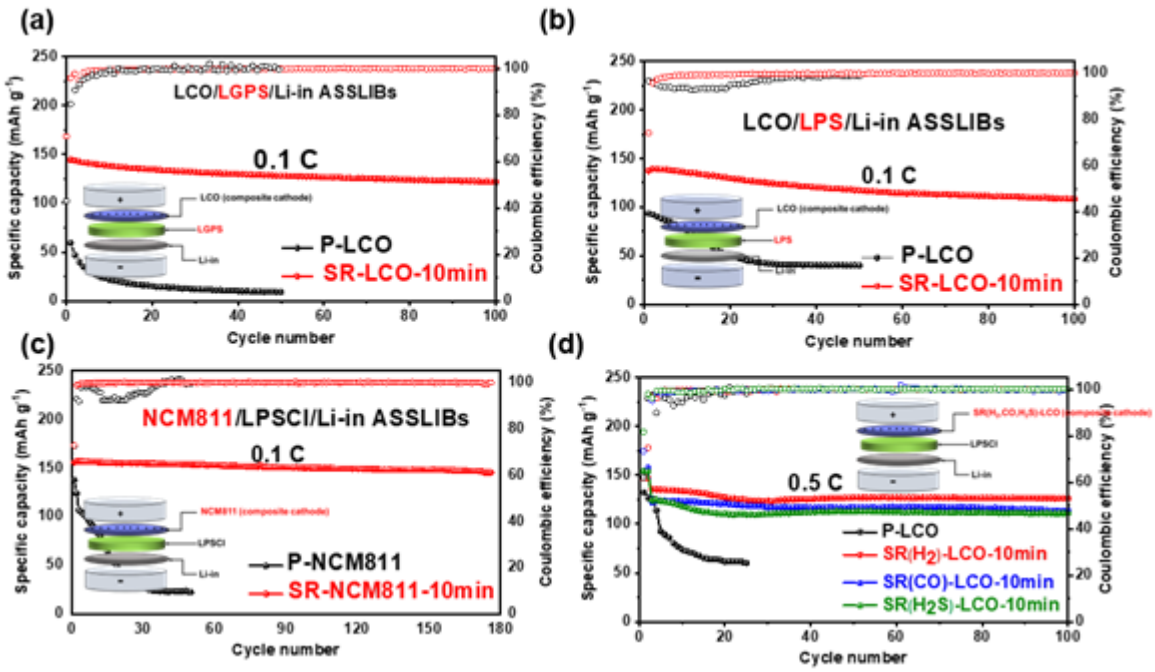

Figure 6. Generality and transferability. (**a**-**b**) The cycling performance of ASSLBs with P-LCO and SR-LCO-10min using LGPS and LPS SE, respectively. (**c**) The cycling performance of ASSLBs with NCM811

before and after GSIRR process. (**d**) The cycling performance of ASSLBs with LCO before and after treatment by various reducing gases (H_2, CO, H_2S) at 0.5C.

It is also a challenge to achieve long-lasting NCM811-based ASSLB cells. GSIRR process was also employed to modify the surface of NCM811 to obtain a stable interface with LPSCl SE. XRD patterns suggest that NiO phase (JCPDS No. 47-1049) is created over the NCM811 surface (**Figure S29**a). Because of the robust NiO phase, the SR-NCM811 (surface reconstructed NCM811) cathodes deliver 155.7 mAh g^{-1} first discharge capacity at 0.1C, with 93.3% capacity retention up to 180 cycles. This ASSLB performance is in strong contrast to that of pristine NCM811 (P-NCM811), which just delivers a discharge capacity of 68.4 mAh g^{-1} at 0.1C and preserves 49.4% capacity after 100 cycles (**Figure 6**c and **Figure S29**b). Much smaller interfacial resistance after 10 cycles further supports the enhancement of interfacial stability (**Figure S29**c). Moreover, the cycling performance of SR-NCM811with different cut-off voltages (from 3.8 to 3.9 and 4.0 V) (**Figure S30**) shows that SR-NCM811 achieves a high capacity retentions of 71.73% after 160 cycles (2-3.9 V) and 75.20% after 115 cycles (2-4 V) at 0.2C, respectively. Thus, the above results suggest that the GSIRR process also enhances the cycling stability of the NCM811 electrode by reengineering interfaces.

It should be pointed out that the other reducing gases may create a similar surface reconstructed layer. To further confirm the generality of the GSIRR method for oxide cathodes, we extended the H_2 gas to other reducing gas, including CO and H_2S. To distinguish GSIRR processed LCO with different reducing gases (H_2, CO, and H_2S), SR-LCO-10min is subdivided into SR(H_2)-LCO-10min, SR(CO)-LCO-10min, and SR(H_2S)-LCO-10min, respectively. **Figure 6**d compares LCO/LPSCl/Li-In ASSLBs using the three different SR-LCO-10min samples. After CO heat reduction, the same CoO/Li_2CO_3 SRL layer would be generated on the LCO surface (**Figure S31**a), evidenced by pronounced CoO diffraction peaks in XRD pattern of SR(CO)-LCO-10min. The thermal reduction by

H_2S would also form the same SRL layer (**Figure S31**b), indicating CoO/Li_2CO_3 SRL layer generation mainly contributes to the heat reduction of LCO no matter the type of reducing gases. After GSIRR process, SR(H_2)-LCO-10min, SR(CO)-LCO-10min, and SR(H_2S)-LCO-10min can deliver similar initial capacities of 146.9 mAh g^{-1}, 153.7 mAh g^{-1}, and 157.8 mAh g^{-1} at 0.1C, respectively. In contrast, P-LCO can only enable a reversible capacity of only 127.1 mAh g^{-1}, indicating an enhanced interface realized by GSIRR process. Besides that, efficient performance enhancement also can be demonstrated by the cycling stability at 0.5C. Observably, high capacity retentions of 93.20%, 93.26%, and 91.13% after 100 cycles can be achieved by heat reduction by H_2, CO, and H_2S, respectively (**Figure 6**d). Relative chare-discharge curves at 0.1C and 0.5C reveal smaller battery polarization after GSIRR process (**Figure S32**a-b).

As for the reaction mechanism and the SRL change when using different reducing gases, we speculate the following mechanism: i) surface oxygen vacancies of CAM are created utilizing a reducing atmosphere and oxygen loss with flowing gas at high temperature, and ii) the surface structure of CAM transforms from layered to rock-salt phase by heat treatment. Different reducing gases would affect the kinetic rate of surface reaction and hence the thickness of surface phase transformation. In conclusion, the universality investigation of the GSIRR method figures out an efficient SRL layer fabrication by the GSIRR process, available in three sulfide-based SEs, providing a scale-up production method toward efficient interface stability improvement. Further studies along this line are needed to check whether GSIRR process will work for more cathode materials.

3. Conclusion

In summary, we have successfully implemented a straightforward yet highly effectve method for surface reconstruction based on GSIRR. This approach was employed to create an in-situ CoO/Li_2CO_3

SRL layer on the LCO cathode, yielding remarkable outomes. The CoO/Li_2CO_3 SRL layer serves a dual purpose: firstly, it mitigates the adverse effects of high electronic energy levels from oxygen or oxidized oxygen species in the cathode, preventing any harm to the sulfide SE. Secondly, it establishes a conducive ion transport layer, effectively eliminating polarization issues. As a result of these advancements, the SR-LCO/LPSCL/Li-In ASSLB cells achieve excellent electrochemical performance, including higher initial discharge capacity, outstanding long cycling performance, much better rate performance, and lower resistance. Impressively, the cells maintain an impressive capacity retention rate of 85% even after undergoing 100 cycles at 0.3 C, all while boasting a high LCO areal loading of 28.97 mg cm^{-2}. Furthermore, we observed that other reducing gas, such as H_2S and CO, yield similar positive effects on the LCO cathode. Moreover, the CoO/Li_2CO_3 SRL layer applied to the LCO also plays a vital role in stabilizing the interface with LGPS and LPS. More importantly, the GSIRR process has been successfully extended to the in-situ formation of NiO on NCM811, leading to enhanced cycling stability for NCM811. Our findings hold promise for the development of a range of transition metal oxides combined with Li_2CO_3, such as layered Ni-Mn-Co or Ni-Co-Al systems. This innovative approach could significantly enhance the compatibility of cathode/SE interfaces in all-solid-state lithium batteries in a cost-effective manner.

4. Experimental Section

Materials: Monocrystal $LiCoO_2$ and monocrystal $LiNi_{0.8}Co_{0.1}Mn_{0.1}O_2$ were provided by Xiamen Tungsten Co., Ltd (XTC). indium foils (100 mm in thickness) were purchased from Canrd New Energy Technology Co., Ltd. Solid electrolytes (Li_6PS_5Cl (LPSCl), b-Li_3PS_4 (LPS), $Li_{10}GeP_2S_{12}$ (LGPS)) were purchased from Hefei Kejing materials technology co., Ltd. Reducing gases (H_2, CO, H_2S) (8 Vol% with

Ar as carrier gas) were provided by Guangzhou Dan Ou Dan Tong Trading Co. Lithium (99.99%, 50 mm in thickness) was brought from China Energy Lithium Co., Ltd.

Material fabrication

Preparation of SR-LCO: P-LCO was conducted in a quartz tube furnace. To more precisely control the SRL layer over LCO, a multi-step thermal procedure was applied. During the temperature increase, the N_2 flux was used as a protective gas. When the temperature rose to 650 °C, the gas was changed to H_2, and a reduction reaction between H_2 and LCO initiates. Following the cooling down process, the gas is changed to N_2 protection gas until reaching room temperature. Precise thickness control of SRL layer over LCO can be adjusted by limiting the holding time of H_2 flux. A series of SR-LCO oxides (denoted as SR-LCO-Xmin, X = 5, 10, 15, 20 minutes) with different GSIRR reaction time with H_2 gas were obtained by controlling sintering time.

Preparation of SR(CO)-LCO and SR(H_2S)-LCO: the SR(CO)-LCO and SR(H_2S)-LCO were synthesized with a similar method to SR(H_2)-LCO by replacing the H_2 with CO or H_2S.

Preparation of SR-NCM811: SR-NCM811 was prepared by using a similar method to SR-LCO by replacing P-LCO with NCM811.

Electrochemical tests

Cells assembling: The cathode for ASSLBs was prepared by mixing the 150 mg cathode, 100 mg solid electrolytes (SEs), and 5 mg acetylene black by hand-milling for over 30 min. Then 10 mg cathode mixtures and 180 mg SEs were pressed into a pellet under 360 MPa (ϕ=13 mm, with ~4.5 mg cm^{-2} active material) for 10 min. An In foil and a Li foil were placed with cathode/SEs pellets followed by

20 MPa to assemble the ASSLBs. All the preparation processes of the ASSLBs mentioned above were carried out in an Ar-filled glovebox (H_2O/O_2 < 0.01 ppm).

Electrochemical tests: The galvanostatic discharge/charge measurements of ASSLBs with LCO cathodes were conducted at a potential range of 2.6–4.3 V vs. Li^+/Li using the battery tester system (LAND, Wuhan) under room temperature (25 °C), and 1C was defined as 120 mA g^{-1}. For the ASSLBs with NCM811 cathodes, a potential range of 2.6–4.3 V vs. Li^+/Li was applied, and 1C was defined as 150 mA g^{-1}. The GITT curves of ASSLBs were performed with a 20 min discharge at 0.2C followed by a 2-hour relaxation. The Cyclic voltammetry (CV) was used to investigate the electrochemical process of ASSLBs, performed at the CHI660E working station (Chenhua, Shanghai) at a voltage range of 2.6–4.3 V vs. Li^+/L at a scan rate of 0.2 mV s^{-1}. The Electrochemical impedance spectroscopy (EIS) of ASSLBs was performed in the Autolab working station (Wantong, Switzerland) with a frequency range from 105 Hz to 0.01 Hz and an AC perturbation signal of 5 mV. Li^+ diffusion coefficient, D_{Li}, was calculated according to equation below:

$$D^{GITT} = \frac{4}{\pi\tau}\left(\frac{m_B V_M}{M_B S}\right)^2\left(\frac{\Delta Es}{\Delta Et}\right)^2 \quad (1)$$

where τ is pulse duration time (1800 s); m_B is mass of LCO; M_B is the molecular weight of LCO (81.87 g/mol); V_m is the molar weight of LCO (32.13 cm^3/mol); S is the area of the interfaces between LCO and sulfide SE: m_B times specific surface area of LCO (0.55 m^2/g); ΔE_s represents the voltage difference between two consecutive steady states; ΔE_τ indicates the voltage change following a single pulse.

Materials characterization: Powder X-ray diffraction (XRD) was carried out on Rigaku Ultima IV, the radiation source was Cu Kα, and the samples were scanned at a 2θ range of 5 to 90° with a scan

speed of 1° min^{-1}. The XRD Rietveld refinement was performed in TOPAS software. A field emission scanning electron microscope (FESEM, Hitachi S-4800) was used to observe the morphologies of cathodes before and after reduction. Fourier-transform infrared spectroscopy (FTIR, Nicolet 8700) was mainly used for the analysis of functional groups in LCO samples. The CoO/Li_2CO_3 SRL layer on the surface of LCO was observed via a high-resolution transmission electron microscope (HRTEM) at an accelerating voltage of about 200 kV. The SR-LCO-10min samples were prepared by a focused ion beam (FIB). Electron energy loss spectroscopy was used in a scanning transmission electron microscope (STEM) to map the distribution of Co^{2+} and Co^{3+} in the samples. A PHI 5000 VB III electron spectrometer (X-ray photoelectron spectroscopy, XPS) was used to surface components of samples and cathode/SEs interface by-products generation, and the binding energies reported herein were corrected regarding C–C/C–H signal at 284.8 eV. An Al Kα monochromatized radiation ($h\nu$ = 1486.6 eV) was employed as an X-ray source. The surface of the specimen is sputtered by inert gas ion bombardment with a sputter rate of 15 nm (SiO_2 as standard reference) for each time, and spectra are then collected from the center of an etched area. Survey spectra were recorded with a pass energy of 0.125 eV, and high-resolution spectra were recorded with a pass energy of 0.02 eV. Peak fitting was performed with the XPS Peak software. The local electronic environment of LCO cathode before and after treatment was determined by the X-ray absorption spectra at American Light source (ALS). The obtained data were analyzed by Athena software. Co K-edge spectra were collected in total electron yield mode. O K-edge XANES spectra of LCO cathode were collected under the total electron yield (TEY) and fluorescence yield (FY) mode at Spherical Grating Monochrometer (SGM) beamline.

Calculation method: All density functional theory (DFT) + U calculations were conducted using first-principles methodology within the Vienna ab initio simulation package (VASP), employing the

projector augmented-wave approach[39]. The generalized gradient approximation (GGA) was used in the scheme of Perdew-Burke-Ernzerhof (PBE) to describe the exchange-correlation functional[40, 41]. The plane-wave cutoff was set to 500 eV. The rotational invariant approach of Dudarev was used[41], where a Coulomb parameter U and exchange parameter J are combined into a single U-J parameter. That is, we referred to U instead of U-J. For 3*d* orbital of Co, the chosen value of U is 3.9 eV V in accordance with the previous theoretical study.[42] For LCO bulk structure, a 4 × 4 × 2 k-point grid was taken. For CoO and LPSCl bulk structures, a 4 × 4 × 4 k-point grid was taken. The interface chemical reactions was generated through the utilization of pymatgen. This process facilitated the identification of phase equilibria for targeted materials and chemical reactions[43,44,45]. For the cathode/solid electrolyte (SE) interface, ab initio molecular dynamics (AIMD) simulations were conducted. We built LCO/LPSCl interface and CoO/LPSCl interface structures considering the most stable surface of LCO and CoO surface. These AIMD simulations were grounded in the GGA-PBE functional, backed by a plane wave energy cutoff of 400 eV, and centered on a Gamma-only k-point sampling strategy. To capture the dynamics with precision, a time step of 2 fs was meticulously selected. The entire molecular dynamics process spanned a comprehensive temporal range of 20 ps, facilitating a comprehensive exploration of the system's behavior. The interface reaction energy of LCO and LSPCl is analyzed after computing the chemical reaction energy (Δ*E*) of LCO or LPSCl with respect to the possible reaction products. Δ*E* is defined as

$$\Delta E(\text{LCO-LSPCl}) = E(\text{reaction products}) - E(\text{LCO}) - E(\text{LSPCl}). \quad (2)$$

The negative value of Δ*E* means the decomposition is favorable.

Acknowledgments

This work was supported by the Province Natural Science Fund of Guangdong (2022A1515012476) and the National Natural Science Foundation of China (Projects 52172190 and 51874104).

Contributions

Z He synthesized all the materials and conducted electrochemical measurements. B Zhang and Z Lin conceived the idea and designed the experiments. W Zhao, Z-W Yin and M Zhang conducted XPS and TEM measurements. Z Zhuo performed XAS analyses. B Zhang, H Zhi, S Zhang, and Z Lin wrote the manuscript and all authors edited the manuscript.

Competing financial interests

The authors declare no competing financial interests.

References

1. Chen, R., Li, Q., Yu, X., Chen, L., Li, H. Approaching practically accessible solid-state batteries: stability issues related to solid electrolytes and interfaces. *Chem. Rev.* **120**, 6820-6877 (2020).

2. Goodenough, JB., Kim, Y. Challenges for rechargeable Li batteries. *Chem. Mater.* **22**, 587-603 (2010).

3. Lin, Z., Liu, T., Ai, X., Liang, C. Aligning academia and industry for unified battery performance metrics. *Nat. Commun.* **9**, 5262 (2018).

4. Randau, S., Weber, DA., Koetz, O., Koerver, R. *et al.* Benchmarking the performance of all-solid-state lithium batteries. *Nat. Energy* **5**, 259-270 (2020).

5. Zhang, Q., Cao, D., Ma, Y., Natan, A., Aurora, P., Zhu, H. Sulfide-based solid-state electrolytes: synthesis, stability, and potential for all-solid-state batteries. *Adv. Mater.* **31**, 1901131 (2019).

6. Yu, C., van Eijck, L., Ganapathy, S., Wagemaker, M. Synthesis, structure and electrochemical performance of the argyrodite Li_6PS_5Cl solid electrolyte for Li-ion solid state batteries. *Electrochim. Acta* **215**, 93-99 (2016).

7. Kato, Y., Hori, S., Kanno, R. $Li_{10}GeP_2S_{12}$-type superionic conductors: synthesis, structure, and ionic transportation. *Adv. Energy Mater.* **10**, (2020).

8. Zhang, B., Tan, R., Yang, L., Zheng, J. *et al.* Mechanisms and properties of ion-transport in inorganic solid electrolytes. *Energy Storage Mater.* **10**, 139-159 (2018).

9. Kamaya, N., Homma, K., Yamakawa, Y., Hirayama, M. *et al.* A lithium superionic conductor. *Nat. Mater.* **10**, 682-686 (2011).

10. Kato, Y., Hori, S., Saito, T., Suzuki, K. *et al.* High-power all-solid-state batteries using sulfide superionic conductors. *Nat. Energy* **1**, (2016).

11. Richards, WD., Miara, LJ., Wang, Y., Kim, JC., Ceder, G. Interface stability in solid-state batteries. *Chem. Mater.* **28**, 266-273 (2016).

12. Lim, H-D., Park, J-H., Shin, H-J., Jeong, J. *et al.* A review of challenges and issues concerning interfaces for all-solid-state batteries. *Energy Stor. Mater.* **25**, 224-250 (2020).

13. Yang, Y., Wu, S., Zhang, Y., Liu, C*. et al.* Towards efficient binders for silicon based lithium-ion battery anodes. *Chem. Eng. J.* **406**, 126807 (2021).

14. Wu, C., Lou, J., Zhang, J., Chen, Z*. et al.* Current status and future directions of all-solid-state batteries with lithium metal anodes, sulfide electrolytes, and layered transition metal oxide cathodes. *Nano Energy* **87**, 106081 (2021).

15. Xiao, Y., Wang, Y., Bo, S-H., Kim, JC., Miara, LJ., Ceder, G. Understanding interface stability in solid-state batteries. *Nat. Rev. Mater.* **5**, 105-126 (2020).

16. Zahiri, B., Patra, A., Kiggins, C., Yong, AXB*. et al.* Revealing the role of the cathode-electrolyte interface on solid-state batteries. *Nat. Mater.* **20**, 1392-1400 (2021).

17. Jung, SH., Oh, K., Nam, YJ., Oh, DY*. et al.* Li_3BO_3-Li_2CO_3: rationally designed buffering phase for sulfide all solid-state Li-ion batteries. *Chem. Mater.* **30**, 8190-8200 (2018).

18. Walther, F., Strauss, F., Wu, X., Mogwitz, B*. et al.* The working principle of a Li_2CO_3/$LiNbO_3$ coating on NCM for thiophosphate-based all-solid-state batteries. *Chem. Mater.* **33**, 2110-2125 (2021).

19. Seino, Y., Ota, T., Takada, K. High rate capabilities of all-solid-state lithium secondary batteries using $Li_4Ti_5O_{12}$-coated $LiNi_{0.8}Co_{0.15}Al_{0.05}O_2$ and a sulfide-based solid electrolyte. *J. Power Sources* **196**, 6488-6492 (2011).

20. Culver, SP., Koerver, R., Zeier, WG., Janek, J. On the functionality of coatings for cathode active materials in thiophosphate-based all-solid-state batteries. *Adv. Energy Mater.* **9**, 1900626 (2019).

21. Nisar, U., Muralidharan, N., Essehli, R., Amin, R., Belharouak, I. Valuation of surface coatings in high-energy density lithium-ion battery cathode materials. *Energy Stor. Mater.* **38**, 309-328 (2021).

22. Chen, J., Deng, W., Gao, X., Yin, S*. et al.* Demystifying the lattice oxygen redox in layered oxide cathode materials of lithium-ion batteries. *ACS Nano* **15**, 6061-6104 (2021).

23. Negi, RS., Yusim, Y., Pan, R., Ahmed, S*. et al.* A dry-processed $Al_2O_3/LiAlO_2$ coating for stabilizing the cathode/electrolyte interface in high-ni ncm-based all-solid-state batteries. *Adv. Mater. Interfaces* **9**, 2101428 (2022).

24. Wang, C., Chen, L., Zhang, H., Yang, Y. *et al.* Li_2ZrO_3 coated $LiNi_{1/3}Co_{1/3}Mn_{1/3}O_2$ for high performance cathode material in lithium batteries. *Electrochim. Acta* **119**, 236-242 (2014).

25. Lu, Z., Chen, G., Li, Y., Wang, H*. et al.* Identifying the active surfaces of electrochemically tuned $LiCoO_2$ for oxygen evolution reaction. *J. Am. Chem. Soc.* **139**, 6270-6276 (2017).

26. You, Y., Celio, H., Li, J., Dolocan, A., Manthiram, A. Modified high-nickel cathodes with stable surface chemistry against ambient air for lithium-ion batteries. *Angew. Chem. Int. Ed.* **57**, 6480-6485 (2018).

27. Seong, WM., Kim, Y., Manthiram, A. Impact of residual lithium on the adoption of high-nickel layered oxide cathodes for lithium-ion batteries. *Chem. Mater.* **32**, 9479-9489 (2020).

28. Wang, C-W., Ren, F-C., Zhou, Y., Yan, P-F*. et al.* Engineering the interface between $LiCoO_2$ and $Li_{10}GeP_2S_{12}$ solid electrolytes with an eltrathin $Li_2CoTi_3O_8$ interlayer to boost the performance of all-solid-state batteries. *Energy Environ. Sci.* **14**, 437-450 (2021).

29. Bi, Y., Yang, W., Du, R., Zhou, J. *et al.* Correlation of oxygen non-stoichiometry to the instabilities and electrochemical performance of $LiNi_{0.8}Co_{0.1}Mn_{0.1}O_2$ utilized in lithium ion battery. *J. Power Sources* **283**, 211-218 (2015).

30. Deng, S., Sun, Q., Li, M., Adair, K. *et al.* Insight into cathode surface to boost the performance of solid-state batteries. *Energy Stor. Mater.* **35**, 661-668 (2021).

31. Deng, S., Li, X., Ren, Z., Li, W. *et al.* Dual-functional interfaces for highly stable Ni-rich layered cathodes in sulfide all-solid-state batteries. *Energy Stor. Mater.* **27**, 117-123 (2020).

32. Alvarado, J., Wei, C., Nordlund, D., Kroll, T. *et al.* Thermal stress-induced charge and structure heterogeneity in emerging cathode materials. *Mater. Today* **35**, 87-98 (2020).

33. Zhang, J., Zheng, C., Li, L., Xia, Y. *et al.* Unraveling the intra and intercycle interfacial evolution of Li_6PS_5Cl-based all-solid-state lithium batteries. *Adv. Energy Mater.* **10**, (2020).

34. Li, X., Sun, Q., Wang, Z., Song, D. *et al.* Outstanding electrochemical performances of the all-solid-state lithium battery using Ni-rich layered oxide cathode and sulfide electrolyte. *J. Power Sources* **456**, (2020).

35. Koerver, R., Walther, F., Ayguen, I., Sann, J. *et al.* Redox-active cathode interphases in solid-state batteries. *J. Mater. Chem. A* **5**, 22750-22760 (2017).

36. Auvergniot, J., Cassel, A., Ledeuil, J-B., Viallet, V., Seznec, V., Dedryvere, R. Interface stability of argyrodite Li_6PS_5Cl toward $LiCoO_2$, $LiNi_{1/3}Co_{1/3}Mn_{1/3}O_2$, and $LiMn_2O_4$ in bulk all-solid-state batteries. *Chem. Mater.* **29**, 3883-3890 (2017).

37. Zhang, W., Richter, FH., Culver, SP., Leichtweiss, T. *et al.* Degradation mechanisms at the $Li_{10}GeP_2S_{12}/LiCoO_2$ cathode interface in an all-solid-state lithium-ion battery. *ACS Appl. Mater. Interfaces* **10**, 22226-22236 (2018).

38. Wang, C., Li, X., Zhao, Y., Banis, MN. *et al.* Manipulating interfacial nanostructure to achieve high-performance all-solid-state lithium-ion batteries. *Small Methods* **3**, (2019).

39. Kresse, G., Furthmüller, J. Efficiency of ab-initiototal energy calculations for eetals and semiconductors using a plane-wave basis set. *Comput. Mater. Sci.* **6**, 15-50 (1996).

40. Perdew., Burke., Ernzerhof. Generalized gradient approximation made simple. *Phys. Rev. Lett.* **77**, 3865-3868 (1996).

41. Dudarev, SL., Botton, GA., Savrasov, SY., Humphreys, CJ., Sutton, AP. Electron-energy-loss spectra and the structural stability of nickel oxide: An LSDA+U study. *Phys. Rev. B* **57**, 1505-1509 (1998).

42. Yang, H., Yang, JY., Savory, CN., Skelton, J. M.; Morgan, *et al.* Highly anisotropic thermal transport in $LiCoO_2$. *J. Phys. Chem. Lett.* **10**, 5552-5556 (2019).

43. Ong, SP., Wang, L., Kang, B., Ceder, G. Li-Fe-P-O_2 phase diagram from first principles calculations. *Chem. Mater.* **20**, 1798-1807 (2008).

44. Ong, SP., Jain, A., Hautier, G., Kang, B., Ceder, G. Thermal stabilities of delithiated olivine MPO_4 (M = Fe, Mn) cathodes investigated using first principles calculations. *Electrochem. Commun.* **12**, 427-430 (2010).

45. Wu, S., Yang, Y., Liu, C., Liu, T. *et al.* In-situ polymerized binder: A three-in-one design strategy for all-integrated siox anode with high mass loading in lithium ion batteries. *ACS Energy Lett.* **6**, 290-297 (2021).

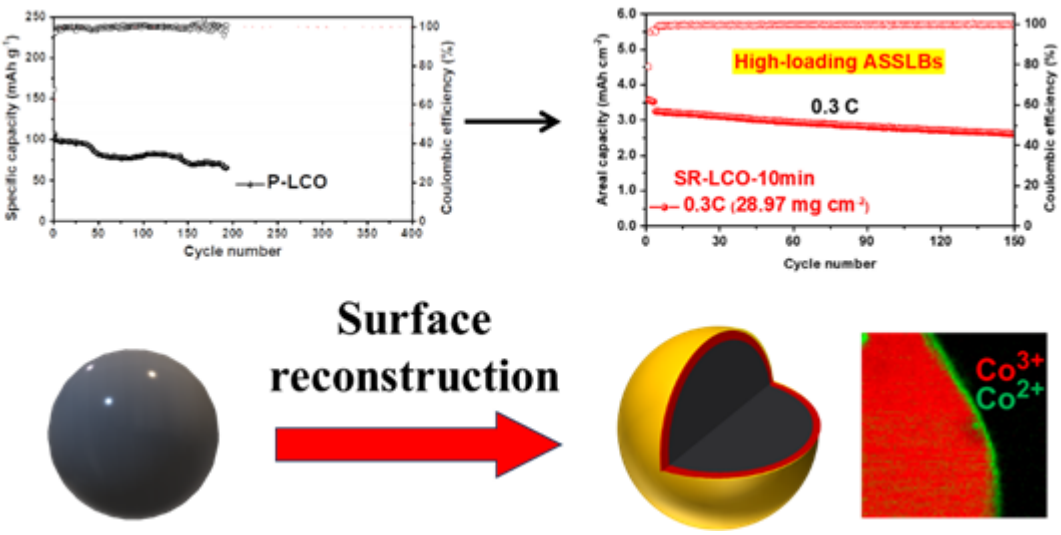

This work highlights the significant influence of surface chemistry of oxide cathode on interfacial compatibility in all-solid-state lithium batteries (ASSLBs). The interface between cathode and solid-state electrolyte is primarily responsible for the prevailing capacity fading and impedance buildup. Therefore, a surface reconstruction strategy based on a gas-solid interface reduction reaction is introduced as a promising avenue for designing enhanced ASSLBs.